Three-dimensional numerical modelling of free convection in sloping porous enclosures

Fernando J. Guerrero-Martínez[a,*], Paul L. Younger[a], Nader Karimi[a]

[a]*School of Engineering, University of Glasgow, Glasgow G12 8QQ, Scotland, UK.*

Abstract

Three-dimensional (3D) numerical simulations are carried out to study steady state free convection in a sloping porous enclosure heated from below. The model is based on Darcy's law and the Boussinesq approximation. Two different approaches to solve this problem are compared: primitive variables and vector potential. Although both numerical models lead to equivalent results in terms of the Nusselt number and convective modes, the vector potential model proved to be less mesh-dependent and also a faster algorithm. A parametric study of the problem considering Rayleigh number, slope angle and aspect ratio showed that convective modes with irregular 3D geometries can develop in a wide variety of situations, including horizontal porous enclosure at relatively low Rayleigh numbers. The convective modes that have been described in previous 2D studies (multicellular and single cell) are also present in the 3D case. Nonetheless the results presented here show that the transition between these convective modes follows an irregular 3D geometry characterized by the interaction of transverse and longitudinal coils.

Keywords: 3D numerical modelling, porous medium, free convection, Boussinesq approximation.

*Corresponding author. Tel.: +44 (0) 141 330 5042

Email address: `f.guerrero-martinez.1@research.gla.ac.uk` (Fernando J. Guerrero-Martínez)

Nomenclature

α	Slope angle
β	Thermal expansion coefficient
$\boldsymbol{\psi}$	Vector potential
$\mathbf{u}$	Dimensionless velocity
κ	Thermal diffusivity
μ	Viscosity
Ω	Surface boundary
ρ_0	Density of reference
θ	Dimensionless temperature
B	Characteristic length
D	Aspect ratio
g	Gravitational constant
k	Permeability
L_∞	Norm infinite
Nu	Nusselt number
P	Dimensionless pressure
Ra	Darcy-Rayleigh number
Ra_c	Critical Rayleigh number
t	Dimensionless time
x, y, z	Dimensionless coordinates

1. Introduction

The problem of free convection in porous media has been of great interest in research due to the widespread presence of this mode of heat transfer in both nature and engineering processes. Geothermal energy and ground water modelling are examples of the application fields of this topic. The problem of a porous enclosure heated from below has been of particular interest for the study of heat transfer rate and steady state convective modes under different parametric conditions. The aim of this paper is to present steady state solutions of free convection in sloping porous enclosures for a range of governing parameters (aspect ratio, slope angle and Rayleigh number) as well as discussing the 3D convective modes present in the parameter space. The steady convection is obtained from the solution of the transient governing equations for long simulation time.

Fundamental aspects of this problem are given by the solution of the Horton-Rogers-Lapwood problem [1]. The solution to this problem establishes the conditions for the onset of convection in a horizontal porous layer heated from below. The early works by Horton and Rogers [2] and Lapwood [3] determined a critical Rayleigh number ($Ra_c = 4\pi^2$) for the onset of convection in such a system. Elder [4] presented one of the first numerical and experimental studies of steady state convection in a two-dimensional (2D) porous enclosure. He described the steady state cellular motion of the fluid, incorporating edge-effects of the porous cavity. Bories and Combarnous [5] extended the analysis to a sloping porous enclosure in 3D following an experimental and theoretical approach. They observed three different kinds of convective regimes, dependent on the model parameters: polyhedral cells similar to the Benard-Rayleigh cells for small slope angles ($\sim 15°$), longitudinal coils (with axis parallel to the longest side of the box) and unicellular flow (which is a 2D velocity distribution) for nearly vertical positions. Regarding the possible convective modes in a horizontal porous enclosure, Holst and Aziz [6] presented one of the earliest numerical models to study this problem in 3D. Considering a set of aspect ratios of a

horizontal porous enclosure they determined the possible convective modes for several Rayleigh numbers. They pointed out that as the 2D motion always satisfies the governing equations, when 3D steady state is possible, then the problem is characterized by a multiplicity of solutions. In a later 3D study by Schubert and Straus [7] the Rayleigh numbers at which 2D and 3D solutions can be steady were examined for the case of a cubic porous enclosure. Horne [8] emphasized that steady flows do not necessarily maximize the energy transfer. When multiple solutions are possible, these early studies agree on the dependence of the resulting steady flow on the initial conditions of the problem. Caltagirone and Bories [9] presented a theoretical and numerical study for a sloping porous box, their results were consistent with the experimental results by Bories and Combarnous [5]. However they also predicted convective regimes characterized by the interaction of longitudinal coils and transverse rolls. More recent research has been carried out by Barletta and Storesletten [10] to study the stability of transverse and longitudinal convective rolls in an inclined porous channel. These authors described the discontinuous nature of the critical Rayleigh numbers as a function of the inclination angle.

Likewise several studies have been carried out in the past to study this problem in 2D. Moya et al. [11] analyzed steady state convection in tilted square and rectangular cavities and the transition between multicellular convective pattern and single cell as the slope angle and Rayleigh-Darcy number were varied, as well as the existence of multiplicity of steady state solutions. Báez and Nicolás [12] studied a wider range of tilt angles and higher Rayleigh numbers as well as several aspect ratios of the porous cavity. They analyzed how the transition angle between single cell and multiple cell is affected by the Rayleigh number. This problem has been further extended to the analysis of entropy generation [13] and also, more recently, to turbulence [14] and non-Darcian effects [15]. Although these recent studies explore new aspects of the physics of the problem, 3D modelling is an important complementary analysis to identify their range of validity. The aim of this work is to illustrate the complexity of the convective modes that can be present in 3D porous enclosures even at low Rayleigh num-

bers, and to highlight the importance of 3D modelling for a better understanding of this problem in real three-dimensional systems.

2. Problem formulation

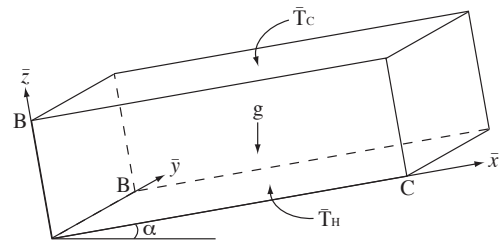

Figure 1: Schematic model of a sloping porous enclosure heated from below and cooled from the top with adiabatic lateral boundaries.

The problem consists of a rectangular porous cavity, tilted at an angle α with respect to the horizontal axis (Figure 1). The porous medium is assumed to be homogeneous and fully saturated. The problem was stated assuming local thermal equilibrium. Fluid flow is described by Darcy's law and buoyancy effects by the Boussinesq approximation. Viscous heat generation is assumed negligible. From these considerations the momentum equation can be stated as follows (the bar notation denotes dimensional variables and operators):

$$\bar{\mathbf{u}} = -\frac{k}{\mu}\left(\bar{\nabla}\bar{P} - \rho_0 g\beta(\bar{T} - \bar{T}_0)\mathbf{e}\right) \tag{1}$$

Where k, μ, ρ_0, β, and g are permeability, viscosity, density of reference, thermal expansion coefficient and gravitational constant, respectively. Likewise $\mathbf{e} = (\sin\alpha, 0, \cos\alpha)$ gives account of the components of the gravity in the system. The energy equation is as follows

$$\frac{\partial\bar{T}}{\partial\bar{t}} + \bar{\mathbf{u}}\cdot\bar{\nabla}\bar{T} = \bar{\nabla}\cdot(\kappa\bar{\nabla}\bar{T}) \tag{2}$$

Where κ is the thermal diffusivity. The condition of incompressibility of the fluid is also invoked:

$$\bar{\nabla} \cdot \bar{\mathbf{u}} = 0 \tag{3}$$

Dimensionless variables are defined as follows:

$$x = \frac{\bar{x}}{B} \quad y = \frac{\bar{y}}{B} \quad z = \frac{\bar{z}}{B} \quad P = \frac{k}{\mu\kappa}\bar{P}$$

$$\mathbf{u} = \frac{B}{\kappa}(\bar{u}, \bar{v}, \bar{w}) \quad \theta = \frac{\bar{T} - \bar{T}_0}{\bar{T}_0 - \bar{T}_c} \quad t = \frac{\bar{t}\kappa}{B^2}$$

$$Ra = \frac{Bkg\beta\rho_0}{\kappa\mu}(\bar{T}_0 - \bar{T}_c)$$

Where Ra is the Darcy-Rayleigh number and B the characteristic length. The dimensionless equations are then as follows, energy equation:

$$\frac{\partial\theta}{\partial t} - \nabla^2\theta + \mathbf{u} \cdot \nabla\theta = 0 \tag{4}$$

The dimensionless momentum equation is as follows:

$$\mathbf{u} + \nabla P = Ra\theta\mathbf{e} \tag{5}$$

The domain is given by $0 \leq x \leq D$, $0 \leq y \leq 1$, $0 \leq z \leq 1$, with $D = C/B$, the aspect ratio. Additionally, a global Nusselt number is defined to quantify the heat transfer through the upper surface $z = 1$:

$$Nu = \int \left| \frac{\partial\theta}{\partial z} \right|_{z=1} dA \tag{6}$$

2.1. Boundary conditions and initial conditions

It is assumed that the system rests at mechanical and thermal equilibrium as the initial condition. Additionally, the initial dimensionless temperature is set to zero. Assuming that the lateral walls of the cavity are adiabatic ($x = 0$, $x = D$, $y = 0$, $y = 1$) and the bottom and top boundaries have specified temperatures, the boundary conditions for the energy equation can be written as

$$\frac{\partial\theta}{\partial x} = 0, \quad \text{for} \quad x = 0 \quad \text{and} \quad x = D$$

$$\frac{\partial \theta}{\partial y} = 0, \quad \text{for} \quad y = 0 \quad \text{and} \quad y = 1$$

$$\theta = 1, \quad \text{for} \quad z = 0 \quad \text{and} \quad \theta = 0, \quad \text{for} \quad z = 1 \quad \text{for} \quad t > 0$$

Regarding the momentum equation impermeable boundary conditions are assumed. The implementation of these boundary conditions is described in the following section.

3. Numerical solution

There are two numerical approaches to solve the problem given above: primitive variables and vector potential. The vector potential approach has been historically preferred [6, 8, 16, 17], since it has proven to be a faster computational algorithm. A comparison of these two methods has not been presented before however.

3.0.1. Primitive variables approach

Taking the divergence of Equation 5 and considering the incompressibility condition, a Poisson equation for the pressure is obtained

$$\nabla^2 P = Ra \left(\frac{\partial \theta}{\partial x} \sin \alpha + \frac{\partial \theta}{\partial z} \cos \alpha \right), \tag{7}$$

Neumann boundary conditions for this Poisson equation are obtained from the momentum equation (Eq. 5). To obtain this Neumann condition let us define the boundary of the enclosure as a surface Ω . Then the pressure gradient normal to the surface must satisfy the following condition [18].

$$\frac{\partial P}{\partial \mathbf{n}}\Big|_{\Omega} = \mathbf{n} \cdot (Ra\theta \mathbf{e} - \mathbf{u})|_{\Omega} \tag{8}$$

The normal component of the velocity is zero in this boundary condition. No restriction is required, however, regarding the tangential velocity (further details of this approach can be referred to Orszag et al. [19] and Karniadakis et al. [20]). This boundary condition ensures mass conservation and leads to

a non-iterative solution algorithm for the problem given by Equations 4 and 7 with the corresponding boundary and initial conditions. The algorithm consists of a three-step procedure per each time step: 1) the energy equation is solved to obtain the temperature field; 2) the Poisson equation is solved; 3) Finally, the velocity field is obtained from Equation 5, for which a second order approximation is applied to calculate the pressure gradient.

The mathematical problem was discretized using the finite volume numerical method [21]. A first order fully implicit scheme was used for temporal discretization which is unconditionally stable. Likewise a central differencing scheme was applied to approximate the convective term in the energy equation.

3.0.2. Vector potential

In the vector potential approach, pressure is eliminated from the momentum equation (Equation 5) by taking the curl. Additionally it is assumed that there exists a solenoidal vector potential, $\boldsymbol{\psi}$, such that $\mathbf{u} = \nabla \times \boldsymbol{\psi}$. So that the curl of Equation 5 leads to:

$$\nabla \times (\nabla \times \boldsymbol{\psi}) = Ra \nabla \times \theta \mathbf{e} \tag{9}$$

And owing to the solenoidal property of $\boldsymbol{\psi}$, it can be simplified as

$$\nabla^2 \boldsymbol{\psi} = -Ra \nabla \times \theta \mathbf{e} \tag{10}$$

The components of this equation are the following:

$$\begin{cases} \nabla^2 \psi_1 = -Ra \frac{\partial \theta}{\partial y} \cos \alpha \\ \nabla^2 \psi_2 = Ra \left(\frac{\partial \theta}{\partial x} \cos \alpha - \frac{\partial \theta}{\partial z} \sin \alpha \right) \\ \nabla^2 \psi_3 = Ra \frac{\partial \theta}{\partial y} \sin \alpha. \end{cases} \tag{11}$$

The corresponding boundary conditions are:

$$\frac{\partial \psi_1}{\partial x} = \psi_2 = \psi_3 = 0, \quad \text{for} \quad x = 0 \quad \text{and} \quad x = D$$

$$\frac{\partial \psi_2}{\partial y} = \psi_1 = \psi_3 = 0, \quad \text{for} \quad y = 0 \quad \text{and} \quad y = 1$$

$$\frac{\partial \psi_3}{\partial z} = \psi_1 = \psi_2 = 0, \quad \text{for} \quad z = 0 \quad \text{and} \quad z = 1$$

The problem given by Equations 4 and 11 and their boundary conditions was also discretized using Finite Volume. This approach requires an iterative solution for each time step for which a fixed point method was implemented. A central differencing scheme was also applied for the convective term of the energy equation and a first-order fully implicit scheme was used for the temporal term. Both algorithms were implemented in Fortran 90 and a Tri-Diagonal Matrix Algorithm (TDMA) with alternating sweep directions was used for the solution of the resulting system of algebraic equations.

As regards the determination of the steady state, it was defined evaluating the convergence of the temperature matrix. The norm infinite of the difference $L_\infty = |\boldsymbol{\theta}^t - \boldsymbol{\theta}^{t-1}|_\infty$ was calculated for successive time steps over a long time interval that proved to be long enough after several tests ($t_{int} = 4.4$). The convergence criterion was defined according to the condition $\langle L_\infty \rangle_{t_{int}} < 5 \times 10^{-7}$, where $\langle L_\infty \rangle_{t_{int}}$ is the average norm infinite over the time interval t_{int}.

4. Numerical results and discussion

4.1. Validation: cubic porous enclosure

The numerical models were validated considering a horizontal cubic cavity ($D = 1$ and $\alpha = 0$). The models were tested just above the critical Rayleigh number ($Ra_c = 39.48$); for this particular test no convergence criterion was used. Instead, a long simulation time was applied ($t = 60$) until significant evidence of convection was detected. Table 1 shows the steady state Nusselt number, both models presented convection at $Ra = 41$ using a coarse mesh composed of $n = 25^3$ elements. With a finer mesh however ($n = 50^3$ elements) the primitive variables model remained conductive ($Nu \simeq 1$).

The steady state Nusselt number was more consistent between the two models when higher Rayleigh numbers were examined. Table 1 shows that identical results were obtained with both models. However, the evolution towards the steady state was different. As shown in Figure 2, primitive variables reaches

Table 1: Nusselt number for a cubic porous enclosure considering two mesh sizes.

		Nu	
Mesh elements	Ra	Primitive variables	Vector potential
$n = 25^3$	40	0.999	0.999
	41	1.070	1.058
$n = 50^3$	40	1.000	1.000
	41	1.000	1.061
$n = 25^3$	60	1.773	1.773
	120	2.934	2.934
$n = 50^3$	60	1.778	1.778
	120	2.945	2.945

the steady state sooner than vector potential. Additionally, primitive variables displayed a higher dependency on the mesh size, whereas the evolution of the Nusselt number in vector potential can be considered mesh-independent. The steady state convective mode in these cases was characterized by a single 2D convective cell.

As regards the time step of these simulations, the optimum time step for the primitive variables model using fine mesh was smaller (10 times) than the other cases studied. The fine mesh primitive variables model required $\Delta t = 2 \times 10^{-5}$ to generate numerically stable results, whereas a time step $\Delta t = 2 \times 10^{-4}$ was

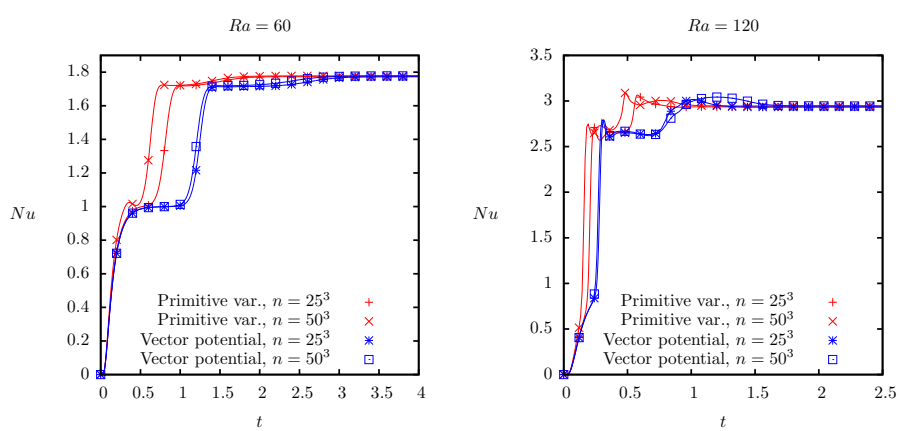

Figure 2: Nusselt number as a function of time for primitive variables and vector potential models using two different mesh sizes ($n = 25^3$ and $n = 50^3$).

suitable in the other cases.

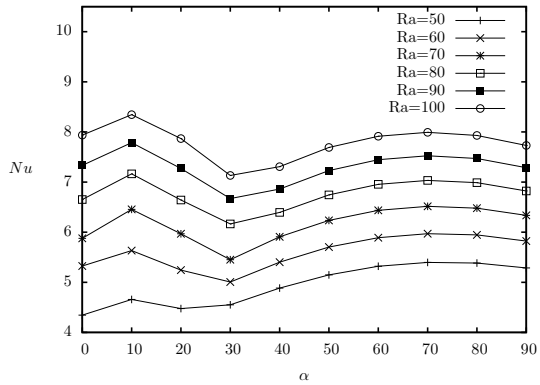

Figure 3: Steady state Nusselt number vs slope angle for an aspect ratio D=3.

Although the models proved a good match with the steady state results for moderate Rayleigh numbers, we opted for the vector potential algorithm for further 3D modelling on the basis that the primitive variables approach is more sensitive to the mesh size and demands a longer computing time when dealing with fine meshes, since the time step required is an order of magnitude smaller.

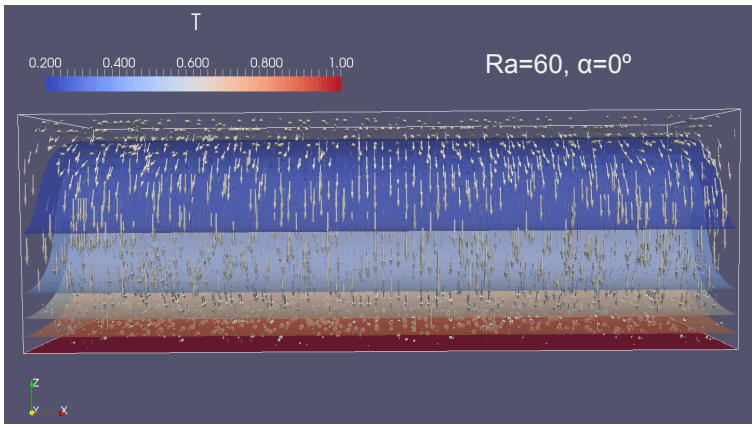

Figure 4: Longitudinal coil characteristic of $\alpha = 0$ and $D = 3$ with $Ra \leq 60$.

4.2. Sloping porous enclosure with aspect ratio $D = 3$

Figure 3 shows the global Nusselt number as a function of the slope angle for a set of Rayleigh numbers, with an aspect ratio $D = 3$. Regarding the horizontal case ($\alpha = 0$), three different convective regimes were observed: a longitudinal coil (Figure 4) for moderate Rayleigh numbers ($Ra \leq 60$), transverse rolls for $Ra \geq 63$ (Figure 5), and the transition between these convective modes for $Ra = 61$ to 62. The transverse rolls regime was characterized either by three or four cells depending on Ra, three cells were observed up to $Ra = 65$ and four cells for higher Ra. The transition between longitudinal coil and transverse rolls for the horizontal box is characterized by an interaction of these convective modes as shown in Figure 6. For this particular case the simulation time required to reach the steady state was $t_{ss} = 9.1$. An additional simulation was carried out for further confirmation of this result using a long simulation time ($t = 60$) without a convergence criterion. The result was the same with a negligible difference in the Nusselt number ($\sim 0.02\%$), this supports the selection of the convergence criterion used to define the steady convection of the system.

As regards the sloping porous enclosure ($\alpha \neq 0$), a local maximum can be identified at $\alpha = 10°$ (Figure 3), which is absolute for $Ra = 80$ and higher.

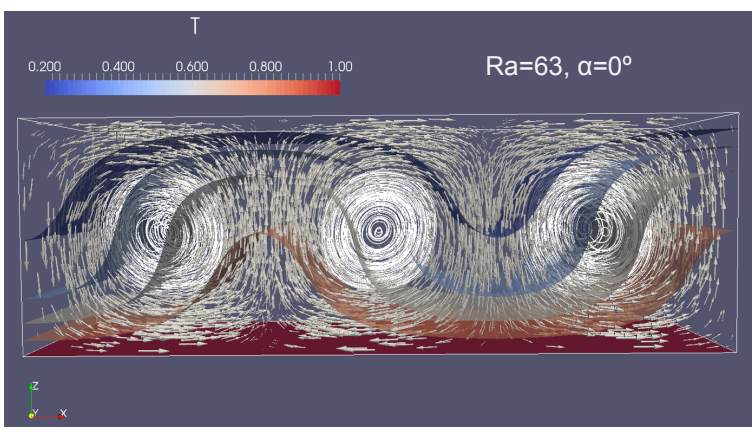

Figure 5: Transverse rolls convective mode for $D = 3$ and $\alpha = 0$. As presented in Table 2, up to 4 cells were observed at higher Rayleigh numbers.

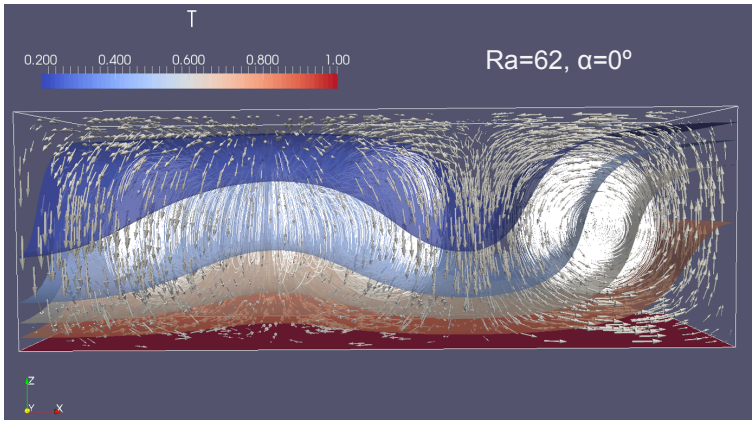

Figure 6: Convective mode characteristic of the transition between the longitudinal coil and transverse rolls for $D = 3$ and $\alpha = 0$.

At this angle the convective flow is characterized by three transverse rolls for every Rayleigh number from 50 to 100 (Figure 7). A summary of results is presented in Table 2. As the angle is increased there is a transition to a single cell regime. Initially, at $\alpha = 20°$, all the cases analyzed undergo a complex 3D velocity distribution (Figure 8) characterized by the interaction of two transverse rolls with a longitudinal coil located in the centre of the box. This convective

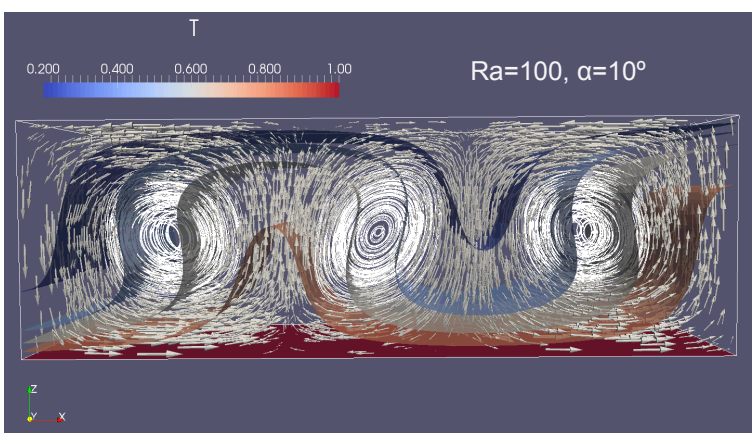

Figure 7: transverse rolls convective mode for $D = 3$, $Ra = 100$, and $\alpha = 10°$. This convective mode provides the maximum heat transfer rate ($Nu = 8.344$) for the parameters considered (Figure 3).

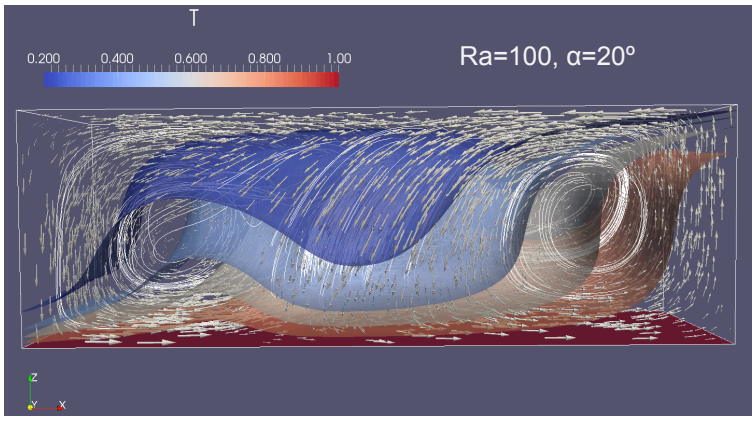

Figure 8: 3D velocity field distribution characteristic of the transition between transverse rolls and single cell convective modes for an aspect ratio $D = 3$.

mode is accompanied by a decrease in the Nusselt number and is consistent with the observations by Caltagirone and Bories [9] who reported an interaction of transverse and longitudinal coils for relatively small slope angles. When the angle is further increased, the convective regime reaches a 2D velocity distribution composed of an external cell with two internal secondary cells (Figure 9). This flow regime has been described in previous 2D studies [12], however, the

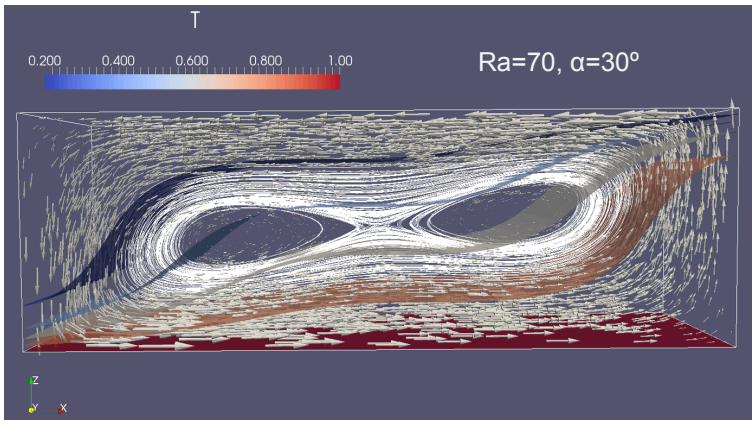

Figure 9: 2D convective mode characteristic of the transition to single-cell convection. The minimum Nusselt number was associated with this convective mode for $Ra = 60$ and higher.

Table 2: Convective modes and transition angles for selected cases.

D	Ra	α	Convective mode	Nu	t_{ss}
3	50	0	longitudinal coil	4.345	9.06
		1	3 transverse rolls	4.399	5.29
		17	transverse rolls with a longitudinal coil	4.507	13.11
		22	external cell with 2 internal secondary cells	4.392	5.16
	100	0	4 transverse rolls	7.936	8.02
		1	5 transverse rolls	7.438	5.39
		6	3 transverse rolls	8.194	19.73
		11	transverse rolls with a longitudinal coil	8.090	14.51
		32	external cell with 2 internal secondary cells	6.871	4.86
5	50	0	longitudinal coil	7.242	9.03
		1	5 transverse rolls	7.295	6.04
		14	transverse rolls with a longitudinal coil	7.264	15.32
		30	external cell with 2 internal secondary cells	6.600	5.09
	100	0	7 transverse rolls	13.119	12.93
		9	partial rotation of transverse rolls	12.905	19.92
		11	transverse rolls with a longitudinal coil	13.263	11.09
		50	single cell	9.846	4.88
10	50	0	transverse rolls with a longitudinal coil	14.336	11.89
		1	11 transverse rolls	14.379	8.50
		10	transverse rolls with a longitudinal coil	14.353	30.76
		30	external cell with 2 internal secondary cells	11.602	4.62
	100	0	14 transverse rolls	26.196	32.78
		1	15 transverse rolls	25.775	8.62
		7	13 transverse rolls	26.656	14.45
		10	partial rotation of transverse rolls	25.493	22.34
		14	transverse rolls with a longitudinal coil	26.092	15.46

3D modelling presented here shows that the transition to this convective mode occurs for a higher α, due to the complex 3D convective mode that is preceding ($\alpha = 20°$). Finally, at $\alpha = 50°$ the convective modes become single cell (Figure 10) with a maximum Nusselt located at $\alpha = 70°$.

4.3. High aspect ratio porous enclosures $D = 5$ and $D = 10$

The parametric study for the aspect ratios $D = 5$ and 10 is shown in Figures 11 and 12, respectively. These figures show that the difference in the Nusselt number at small and large angles increases with the aspect ratio. This is due to the fact that a larger number of convective cells can be hosted in the transverse rolls regime characteristic of small slope angles, the multiplication of up-flow and

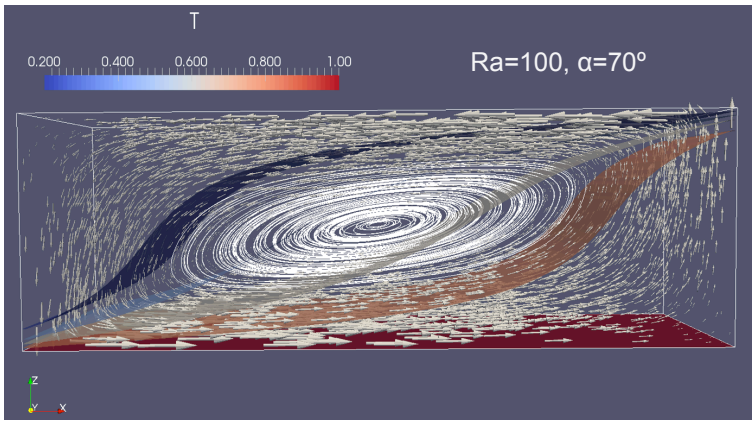

Figure 10: Single cell convective mode for $D = 3$ characteristic of high slope angles.

down-flow zones enhances the heat transfer rate throughout the cavity. Firstly, let us discuss the horizontal case ($\alpha = 0$) for $D = 5$. A longitudinal coil was observed at this aspect ratio for $Ra \leq 62$ (Figure 13), which is characterized by a high up-flow and down-flow areas in comparison with the single cell regime typical of high α; for this reason the Nusselt number turns out to be higher even for moderate Ra (see for instance $Ra = 60$, Figure 11). The transition to transverse rolls in the horizontal case starts at $Ra = 63$ with an interaction of a longitudinal coil and transverse rolls. Unlike $D = 3$ this convective mode proved

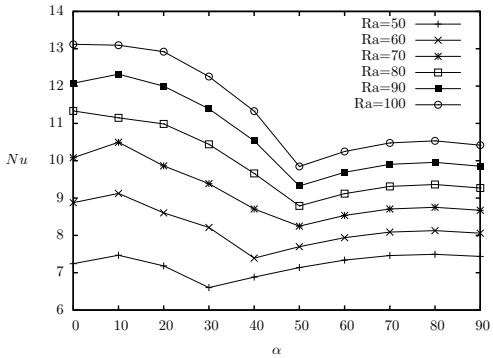

Figure 11: Steady state Nusselt number vs slope angle for an aspect ratio $D = 5$.

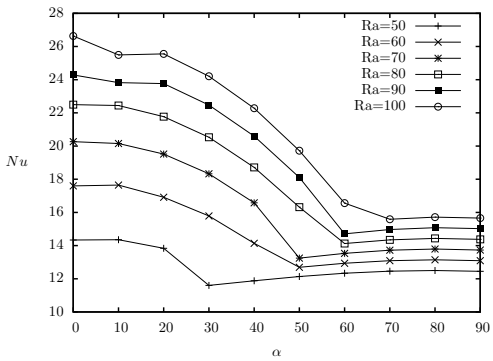

Figure 12: Steady state Nusselt number vs slope angle for an aspect ratio $D = 10$.

to be steady for a wider range of Rayleigh numbers, $Ra = 70$ was characterized by the same convective mode and transverse rolls were only observed at $Ra = 80$ and higher (Figure 13). On the other hand, as regards the horizontal case for the

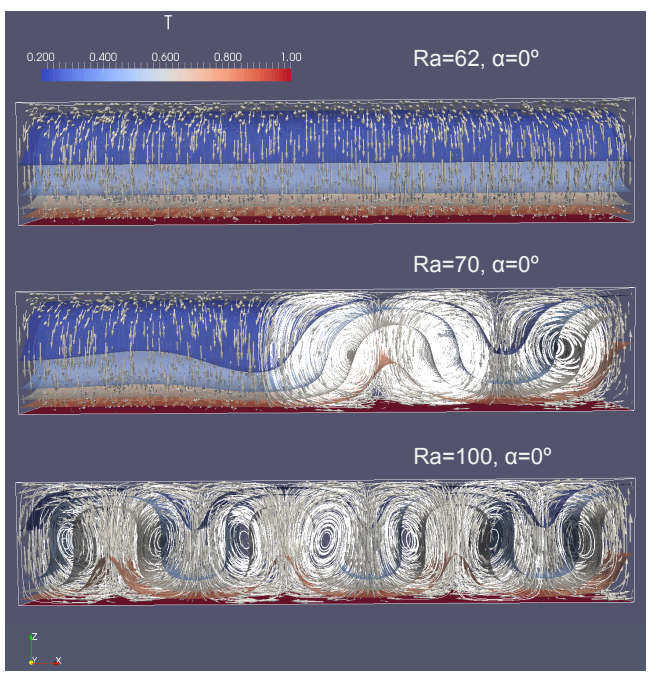

Figure 13: Convective modes characteristic of a horizontal porous enclosure with $D = 5$. As the Rayleigh number is increased the longitudinal coil regime becomes multicellular.

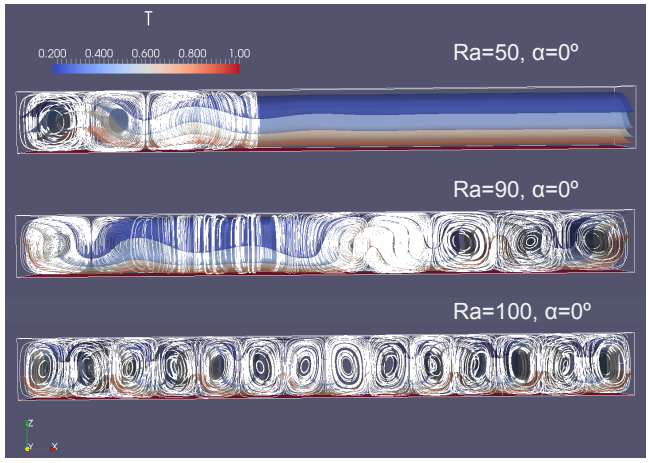

Figure 14: Convective modes characteristic of a horizontal porous enclosure with $D = 10$. A purely longitudinal coil was not attained for this aspect ratio for the Rayleigh numbers considered.

aspect ratio $D = 10$, the steady state was characterized either by the interaction of longitudinal coil and transverse rolls or by a fully transverse rolls regime (Figure 14). Similar arguments apply to explain the high Nusselt number of these cases.

Considering the sloping case for $D = 5$ at $Ra = 50$, three transition angles were identified: $\alpha = 1°$, $\alpha = 14°$, and $\alpha = 30°$ (Figure 15, Table 2). The transition in the convective mode was characterized by a gentle variation in the Nusselt number with the maximum at $\alpha = 80°$ (Nu=7.493) (Figure 11) in response to the low Rayleigh number of the system. At $Ra = 100$, on the other hand, the maximum Nusselt number corresponds to $\alpha = 0$ (Nu=13.119), which is transverse rolls convection. The transition to single-cell convection starts at $\alpha = 9°$, with a partial rotation of the cells located in the centre of the cavity (Figure 16-upper), this rotation leads to the coalescence of these cells giving rise to a longitudinal coil that interacts with transverse rolls ($\alpha = 11°$). Single-cell convection is finally attained at $\alpha = 50°$ after a steep decrease in the Nusselt number.

Similarly, three transition angles were identified for $D = 10$ and $Ra = 50$:

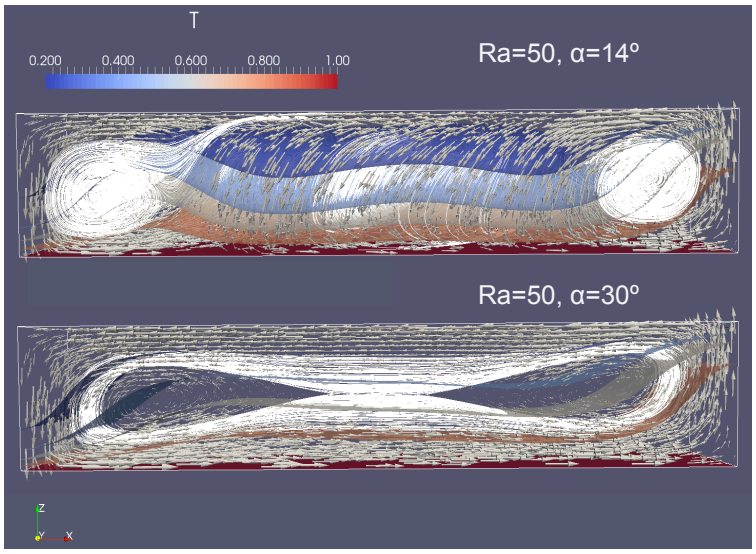

Figure 15: Steady state convective modes for $D = 5$ and $Ra = 50$. $\alpha = 14°$ and $\alpha = 30°$ represent transition angles (Table 2).

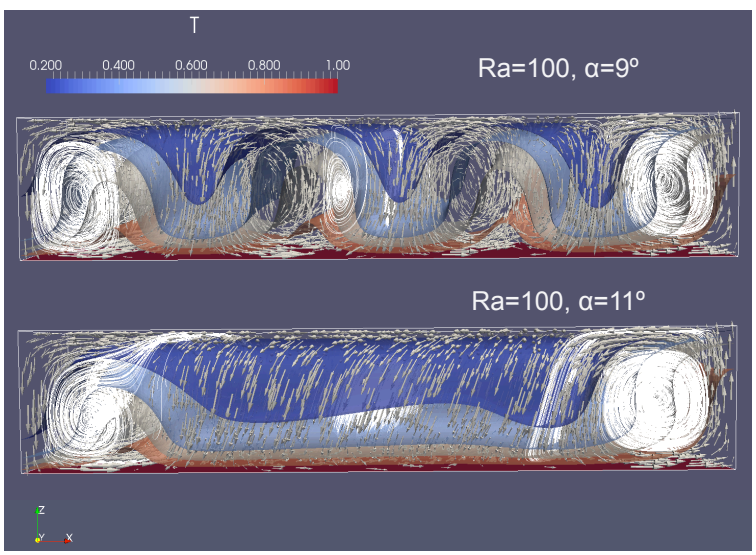

Figure 16: Steady state convective modes for $D = 5$ and $Ra = 100$. $\alpha = 9°$ and $\alpha = 11°$ are transition angles for $Ra = 100$ (Table 2).

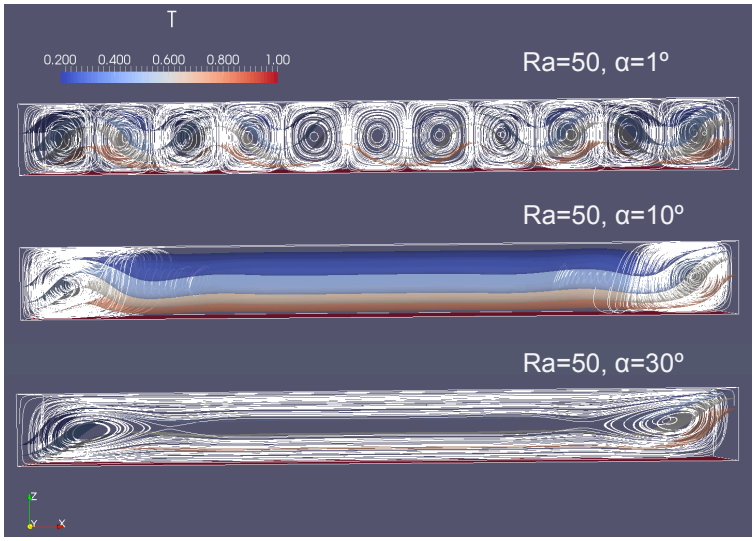

Figure 17: Steady state convective modes for $D = 10$ and $Ra = 50$ at the transition angles (Table 2).

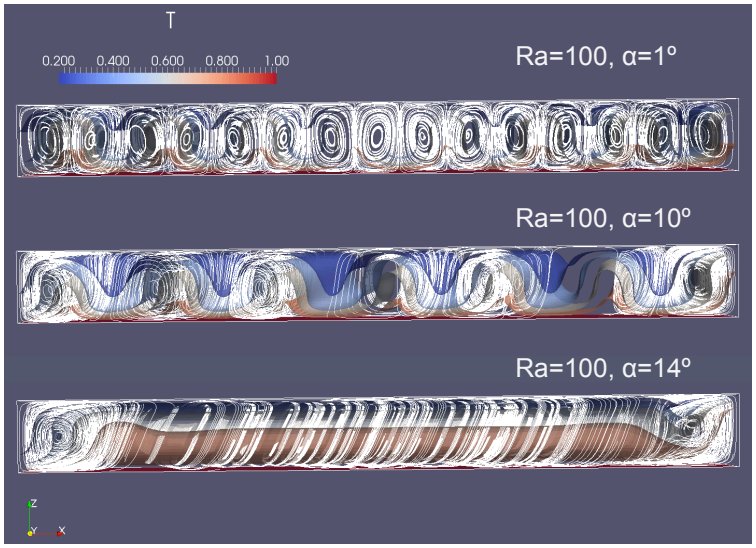

Figure 18: Steady state convective modes for $D = 10$ and $Ra = 100$ at the transition angles (Table 2).

$\alpha = 1°$, $\alpha = 10°$, and $\alpha = 30°$, that correspond to transverse rolls, mixed transverse rolls with a longitudinal coil, and single cell with secondary cells, respectively (Figure 17). At $Ra = 100$ the convective mode remains multicellular until $\alpha = 10°$ (Figure 18). At this angle the transition to single cell starts in the same manner as $D = 5$, the innermost cells coalesce to give rise to a longitudinal coil that interacts with two remaining 2D rolls. For the space of parameters analyzed, the steady state velocity field is no longer two-dimensional until $\alpha = 70°$ where the flow is single cell.

5. Conclusion

Three dimensional numerical simulations were carried out for the study of free convention in sloping porous enclosures. Two different approaches to solve the problem were compared: primitive variables and vector potential. In general terms, both models are suitable to study this problem. However, some limitations were identified in the primitive variables approach. Regarding the sensitivity of the model to the critical Rayleigh number for the onset of convection, it appeared that both models were equally sensitive to the Ra_c when using coarse meshes. When fine meshes were used however, the primitive variables model remained mainly conductive for $Ra = 41$, which is above the critical limit, whereas the vector potential solution was clearly convective. Furthermore, the time step required by primitive variables with a fine mesh was considerably smaller than the time step needed for vector potential, which results in a longer computing time for equivalent simulations. It was also observed that the primitive variables model produced mesh-dependent results, whereas vector potential was mesh independent.

A parametric study for moderate Rayleigh numbers (between 50 and 100) in a sloping porous enclosure permitted us to identify steady state convective modes overlooked by 2D analysis, such as longitudinal coils in the horizontal case and mixed longitudinal coils with transverse rolls, which was observed at Rayleigh numbers as low as 50. A purely longitudinal coil flow was observed

only in the horizontal porous enclosure for low Ra and moderately high aspect ratios, $D = 3$ and $D = 5$. This convective flow was steady in both cases up to a Rayleigh number $Ra \sim 62$, above which occurs a transition to a multicellular regime. The stability of this solution is however affected for higher aspect ratios, since $D = 10$ did not attain a purely longitudinal coil regime. Regarding the case of the sloping enclosure, there is a general tendency to maximize the heat flux with the transverse rolls regime due to the multiplication of up-flow and down-flow regions. For low D and Ra however, the Nusselt number associated with the single cell regime, characteristic of high slope angles, can be comparable or higher. On the other hand, the transition between transverse rolls and single cell convective modes was characterized by a mixed multicellular and longitudinal coil convective flow accompanied by a decrease in the Nusselt number. There is an angle at which transverse rolls are no longer steady. At $Ra = 50$ the transition angle was clearly dependent on the aspect ratio: $\alpha = 17°$, $\alpha = 13°$, and $\alpha = 9°$ were the transition angles for $D = 3$, $D = 5$, and $D = 10$, respectively. For $Ra = 100$ however, that dependency is no longer present, being the transition angle between 9 and 11 for the three aspect ratios analyzed. A more detailed study of the parameter space would be necessary to describe more accurately the transition between the different convective modes observed, for which faster simulations would be convenient. As a final remark, the results show that convective modes in 3D can be of considerable complexity, which impacts not only on the heat transfer properties of the system but also on other aspects not covered so far in this study such as mass transport properties and entropy generation.

Acknowledgements

The first author wants to thank Consejo Nacional de Ciencia y Tecnología (CONACyT) and Cluff Geothermal Ltd. for sponsoring this project. We are grateful to anonymous reviewers for helping us improve our presentation.

References

[1] D. A. Nield, A. Bejan, Convection in Porous Media, 4th ed., Springer, New York, 2013.

[2] C. Horton, F. Rogers, Convection currents in a porous medium, Journal of Applied Physics 16 (1945) 367–370.

[3] E. Lapwood, Convection of a fluid in a porous medium, Proceedings of the Cambridge Philosophical Society 44 (1948) 508–521.

[4] J. Elder, Steady free convection in a porous medium heated from below, Journal of Fluid Mechanics 27 (1967) 29–48.

[5] S. A. Bories, M. A. Combarnous, Natural-convection in a sloping porous layer, Journal of Fluid Mechanics 57 (1973) 63–79.

[6] P. H. Holst, K. Aziz, Transient three-dimensional natural-convection in confined porous media, International Journal of Heat and Mass Transfer 15 (1972) 73–90.

[7] G. Schubert, J. Straus, Three-dimensional and multicellular steady and unsteady convection in fluid-saturated porous-media at high Rayleigh numbers, Journal of Fluid Mechanics 94 (1979) 25–38.

[8] R. N. Horne, Three-Dimensional natural-convection in a confined porous-medium heated from below, Journal of Fluid Mechanics 92 (1979) 751–766.

[9] J. P. Caltagirone, S. Bories, Solutions and stability criteria of natural convective flow in an inclined porous layer, Journal of Fluid Mechanics 155 (1985) 267–287.

[10] A. Barletta, L. Storesletten, Thermoconvective instabilities in an inclined porous channel heated from below, International Journal of Heat and Mass Transfer 54 (2011) 2724–2733.

[11] S. L. Moya, E. Ramos, M. Sen, Numerical study of natural-convection in a tilted rectangular porous material, International Journal of Heat and Mass Transfer 30 (1987) 741–756.

[12] E. Báez, A. Nicolás, 2D natural convection flows in tilted cavities: Porous media and homogeneous fluids, International Journal of Heat and Mass Transfer 49 (2006) 4773–4785.

[13] A. C. Baytas, Entropy generation for natural convection in an inclined porous cavity, International Journal of Heat and Mass Transfer 43 (2000) 2089–2099.

[14] P. H. S. Carvalho, M. J. S. de Lemos, Turbulent free convection in a porous square cavity using the thermal equilibirum model, International Communications in Heat and Mass Transfer 49 (2013) 10–16.

[15] K. Khanafer, Fluid-structure interaction analysis of non-Darcian effects on natural convection in a porous enclosure, International Journal of Heat and Mass Transfer 58 (2013) 382–394.

[16] A. J. Harfash, Three-Dimensional Simulations for Convection Problem in Anisotropic Porous Media with Nonhomogeneous Porosity, Thermal Diffusivity, and Variable Gravity Effects, Transport in Porous Media 102 (2014) 43–57.

[17] D. R. Hewitt, J. A. Neufeld, J. R. Lister, High Rayleigh number convection in a three-dimensional porous medium, Journal of Fluid Mechanics 748 (2014) 879–895.

[18] E. Báez, A. Nicolás, From cat's eyes to multiple disjoint natural convection flow in tall tilted cavities: A direct primitive variables approach, Physics Letters A 377 (2013) 2270–2274.

[19] S. A. Orszag, M. Israeli, M. O. Deville, Boundary conditions for incompressible flows, Journal of Scientific Computing 1 (1986) 75–111.

[20] G. E. Karniadakis, M. Israeli, S. A. Orszag, High-order splitting methods for the incompressible navier stokes equations, Journal of Computational Physics 97 (1991) 414–443.

[21] H. K. Versteeg, W. Malalasekera, An Introduction to Computational Fluid Dynamics, The Finite Volume Method, Prentice Hall, 1995.